International Journal of Mechanical Sciences 248 (2023) 108228

Contents lists available at ScienceDirect

International Journal of Mechanical Sciences

journal homepage: www.elsevier.com/locate/ijmecsci

An additively manufactured manifold-microchannel heat sink for high-heat flux cooling

Daeyoung Kong [a], Euibeen Jung [a], Yunseo Kim [a], Vivek Vardhan Manepalli [b], Kyupaeck Jeff Rah [c], Han Sang Kim [c], Yongtaek Hong [c], Hyoung Gil Choi [c], Damena Agonafer [b], Hyoungsoon Lee [a,d,1,*]

[a] Department of Intelligent Energy and Industry, Chung-Ang University, Seoul 06974, South Korea
[b] Department of Mechanical Engineering, University of Maryland, College Park, MD 20742, USA
[c] Global Technology Center, Samsung Electronics Co., Ltd., Suwon 16677, South Korea
[d] School of Mechanical Engineering, Chung-Ang University, Seoul 06974, South Korea

ARTICLE INFO

Keywords:
Additive manufacturing
Laser powder bed fusion
Manifold microchannel
Electronics cooling
Thermal management

ABSTRACT

Active liquid cooling technique with great efficiency not only reduces power consumption but also effectively dissipates high heat flux. In this study, a manifold-microchannel heat sink (MMCHS) was monolithically fabricated by additive manufacturing, and the thermal and hydraulic performance was investigated in a closed loop. Utilizing AlSi10Mg powder, the laser powder bed fusion process was used to fabricate the complex heat sink structure by directly putting a 3D liquid routing manifold structure on a typical microchannel. The MMCHS, with an overall size of 30 × 15 × 9 mm^3, can support a heated area of 10 × 10 mm^2 and features a tapered structure to facilitate uniform coolant flow. This system contains microchannels with a width and height of 0.2 mm and 2 mm, respectively, with an aspect ratio of AR = 21. Our results show that the MMCHS can dissipate effective heat flux up to 240 W/cm^2 with a mass flow rate of 395 g/min with a considerably low-pressure drop of 1.7 kPa and low heated surface temperature of 100 °C. The corresponding total thermal resistance is as low as 0.21 K/W. In addition, numerical simulations showed detailed flow information as well as good agreement with experimental data. Finally, methods for structural improvement of the manifold microchannel were suggested based on the experimental and numerical results.

1. Introduction

With the rising demands and stringent consumer requirements in the fields of cloud computing, 5G/edge computing, power electronics, and RF communications, industry and research have moved towards the miniaturization of electronics, while simultaneously making them extremely powerful [1]. However, these technological advances encountered significant thermal management issues owing to high heat dissipation, extremely high heat fluxes at hotspot, and increased chip temperature, which leads to sub-optimal electrical performance [2,3]. Hence, efficient thermal management solutions, in the compact form are crucial for the stable and continuous performance of chips. Liquid cooling [4–6] is regarded as a superior cooling method owing to its enhanced heat transfer performance compared to conventional air cooling. Therefore, several studies have been conducted to improve the thermal performance of liquid cooling through different methods such as microchannel cooling [7–12], micro-pin fin cooling [13–19], jet impingement [20–27], spray cooling [28–34], and nanofluids [35–40]. However, these cooling schemes result in a substantially high pressure drop for the flow rate required in the relatively small flow area, and therefore lower energy efficiency.

A manifold-microchannel heat sink (MMCHS) has been proposed to reduce pressure drop in the microchannel while maintaining or even enhancing heat transfer performance. This is achieved by adding a manifold layer on top of the existing microchannel heat sink, leading to an aflow path that is relatively shorter than that of a conventional microchannel [41]. Therefore, MMCHS can use considerably smaller microchannels than conventional heat sinks while operating at a reduced pressure drop and corresponding low pumping power. In addition, a reduced thermal boundary layer thickness and corresponding higher thermal performance can be achieved because of the vertical

* Corresponding author at: Department of Intelligent Energy and Industry, Chung-Ang University, Seoul 06974, South Korea.
E-mail address: leeh@cau.ac.kr (H. Lee).
[1] Website: http://atsla.cau.ac.kr

https://doi.org/10.1016/j.ijmecsci.2023.108228
Received 2 October 2022; Received in revised form 13 February 2023; Accepted 13 February 2023
Available online 16 February 2023
0020-7403/© 2023 Elsevier Ltd. All rights reserved.

Nomenclature

C_p	specific heat
COP	coefficient of performance
D_h	hydraulic diameter
g	gravitational acceleration
H	height
h	convective heat transfer coefficient
k	thermal conductivity
L	total chip length
$\dot{m}$	mass flow rate
P_{pump}	pumping power
ΔP	pressure drop
q	heat dissipation rate
q''	heat flux
R	thermal resistance
Re	Reynold number
T	temperature
t	thickness
u	fluid velocity
V	volumetric flow rate
W	width

Greek symbols

Γ	effective diffusivity
μ	dynamic viscosity
ρ	density
ω	specific dissipation rate

Subscripts

b	bottom
ch	channel
eff	effective
fin	fin
in	inlet
k	turbulence kinetic energy
m	manifold
max	maximum
out	outlet
p	pump
tot	total
w	wall

impingement jet generated between the manifold structure and the microchannel. Thus, MMCHS design has been extensively studied in the last two decades [42–46]. Wang and Ding [42] fabricated a heat spreader by etching and electrodepositing a manifold and microchannels with $W_{ch} = 100$ μm and $H_{ch} = 20$ μm using a silicon wafer as a substrate. They found that the thermal boundary layer developed in a transverse microchannel, and the increased heat transfer area yielded high local heat transfer efficiency, thus demonstrating a uniform temperature distribution. They achieved a thermal resistance of 1.83 K/W with a low flow rate of 6.79 mL/min and a maximum heat flux of 18.9 W/cm^2 in a heating area of 19.4 × 9.1 mm^2. Escher et al. [43] fabricated a compact MMCHS through microfabrication using a silicon substrate and conducted an experimental parametric study of the shape and operating conditions. A novel tapered inlet and outlet ensured constant pressure gradients across the microchannel inside their heatsink, resulting in uniform fluid distribution and temperature uniformity. Using an optimal MMCHS design, a possibility to remove the heat flux of 700 W/cm^2, corresponding to the thermal resistance of 0.023 K/W, was demonstrated at a flow rate of 1.3 L/min using water as a working fluid in a footprint area of 20 × 20 mm^2, to obtain a pressure drop of 22 kPa. They also suggested that the decoupling of flow distribution from the intrinsic heat transfer would help to optimize the design because the optimum design could be shifted by changing the working fluid. Andhare et al. [44] designed and fabricated a multi-pass manifold-microchannel heat exchanger with a large area of 280 × 57 mm^2 using nickel microchannels and PTFE manifolds. They utilized a counterflow to increase the efficiency of the heat exchanger and demonstrated the overall heat transfer coefficient of 20,000 W/m^{2}K at a maximum flow rate of 1.2 L/min using water as a working fluid. Jung et al. [45] fabricated an embedded manifold microchannel using the bonding of two silicon substrates and demonstrated its thermal and hydraulic performance using single-phase water cooling. They introduced a tapered entrance to reduce the pressure drop caused by sudden contractions at the entrance of the plenum, resulting in a 60% pressure drop to approximately 2.6 kPa at a flow rate of 0.1 L/min, and obtained heat flux dissipation of 250 W/cm^2. In addition, the numerical analysis demonstrated the possibility of removing 850 W/cm^2 of heat flux in a single-phase, at the same flow rate. van Erp et al. [46] monolithically fabricated microchannels and manifolds on a single silicon substrate as an embedded cooling module using microfabrication. An ADC converter using GaN was fabricated in a footprint area of about 2.8 × 2.8 cm^2 and approximately 1700 W/cm^2 was dissipated, at a flow rate of 0.06 L/min, resulting in a pressure drop of 125 kPa. They experimentally demonstrated that the electrical-thermal co-design can achieve a cooling effect that exceeds a heat flux of 1 kW/cm^2. The above researchers enhanced the thermal performance and reduced hydraulic loss on their methods, but MMCHS has certain disadvantages; it is still morphologically complex because of its 3D structure and is challenging to design and manufacture because of its numerous design parameters and high manufacturing level, especially in an electronics application.

Additive manufacturing (AM) technology can easily help to manufacture complex 3D structures of MMCHS using computer-aided design tools compared to conventional machining methods like milling, casting, and forming [47–49]. In addition, it has the ability to create rough surfaces or porous media intentionally in order to enhance the permeability of the structures or improve the boiling heat transfer by adjusting the fill ratio and making the lattice structures [50–54]. Arie et al. [55] fabricated an air-to-water manifold-microchannel heat exchanger with Ti alloy through laser powder bed fusion (LPBF) AM technology. They experimentally obtained an airside pressure drop of less than 100 Pa and a Reynolds number range lower than 100 for heat exchange of up to 900 W. Their results suggested that additive manufacturing could be a key role in complex designs which are difficult to fabricate with conventional technologies. Zhang et al. [56] fabricated a nitrogen-to-air manifold-microchannel heat exchanger made of Inconel 718 using the LPBF method. They demonstrated that additive manufacturing could well be utilized to produce compact and lightweight heat exchangers, providing benefits in situations where space and weight are limited. Thus, they improved the heat transfer density by 25% compared to that of conventional fin heat exchangers and achieved a heat exchange of up to 2.78 kW. There were efforts to applicate to microfluidics for the thermal management of electronics as well. Collins et al. [57] designed the manifold microchannel including the straight microchannel using AlSi10Mg. They observed the early flow transition from laminar to turbulent behavior at the Reynolds number of 800 due to the high roughness of AM process. The incorporation of a manifold showed a reduced pressure drop by 90%. Moreover, Collins et al. [58] designed and fabricated a permeable membrane microchannel heat sink using LPBF with aluminum alloy (AlSi10Mg). In their experiment, the intentional porous walls acted both as conducting fins and allowed through-flow for efficient heat transfer, thus a significantly low-pressure drop of approximately 4 kPa was obtained for heat dissipation up to 200

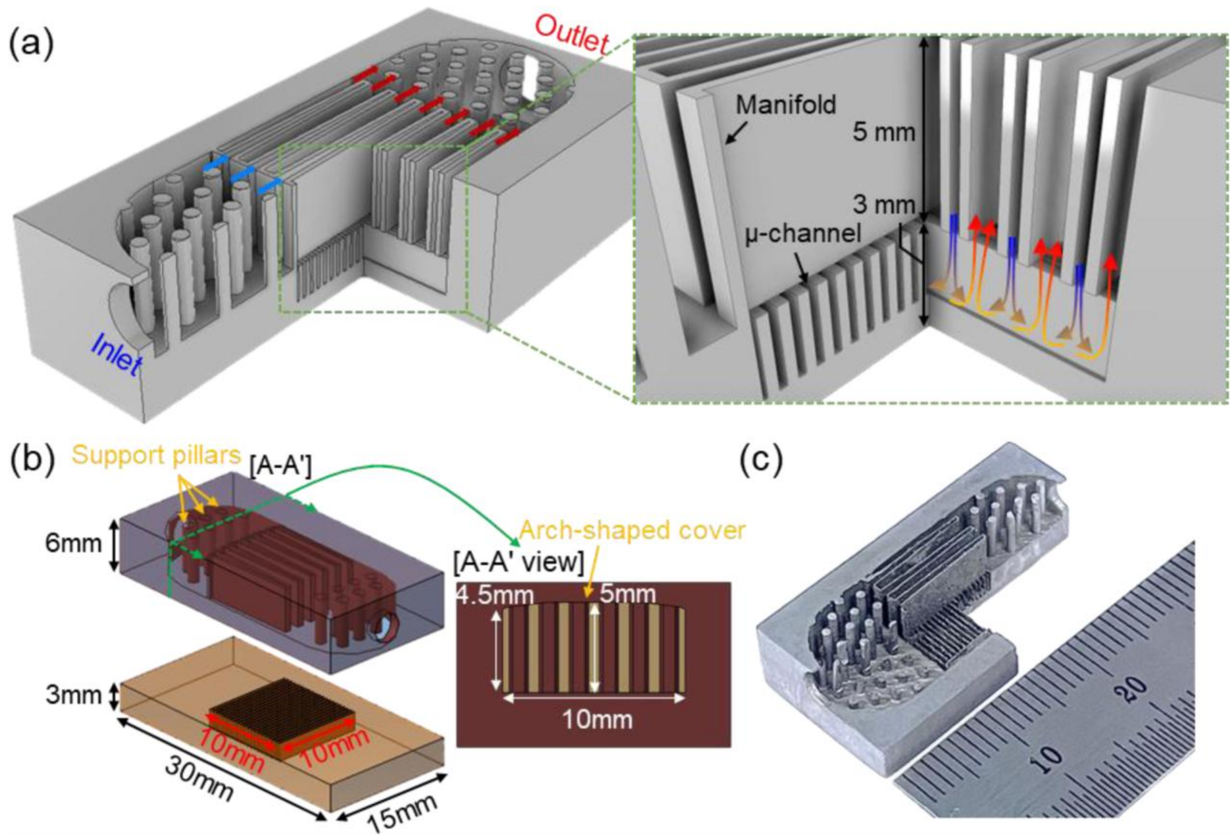

Fig. 1. Additively manufactured manifold microchannel microcooler configurations. (a) The manifold consists of six inlet conduits and seven outlet conduits, and the microchannel has a high aspect ratio with a channel width of 200 μm and height of 2 mm. (b) Support pillars and arch-shaped cover on the top surface are modeled to avoid overhang during the AM process. (c) An additively manufactured MMCHS using AlSi10Mg powders.

W at a flow rate of 500 mL/min using water as the working fluid. They argued that the permeable design from additive manufacturing could produce complex geometries incorporating locally porous features, otherwise unobtainable through conventional manufacture. Kemper et al. [59] fabricated an impinged multijet heat sink using VALLOY-120 and characterized the thermofluidic performances at a high heat flux of 1000 W/cm^2. Due to the superior single-phase heat transfer coefficient, they achieved a six-fold improvement over typical microchannel heat sinks, while concurrently requiring a pressure drop of up to 160 kPa.

Despite the efforts of previous studies, since there is still a need to dissipate high power density consuming low pumping power, we expand the research field to additive manufacturing of microfluidic devices considering the energy-efficient thermal management solutions as well as the fabrication difficulty for the high-powered chip cooling [60]. The objective of this study is to manufacture a compact MMCHS with an area of 10 × 10 mm^2 and a minimum wall thickness of 0.3 mm using AM technology and evaluate its thermal fluid performance using single-phase water cooling. This compact MMCHS was fabricated using LPBF technology, and the experiment was conducted by characterizing the flow rate in the range of $\dot{m} = 100$–400 g/min with a maximum heat flux of $q'' = 240$ W/cm^2 in order to exploit the contribution of flow rate and heat flux to thermal performance. Moreover, the internal streamlines, flow distribution, and ratio of pressure drop were investigated through CFD simulation in order to discuss the hydraulic behavior of MMCHS. This study can contribute to research on the fabrication and performance analysis of AM-based microfluidic cooling devices.

2. Experimental method

The main focus of this study is to develope a compact and robust design of an efficient microcooler using AM technology, as well as its thermal capability. To explore the manufacturability through the LPBF method and to evaluate the single-phase heat transfer in MMCHS, the design of the overall test section, including the fabrication of the microcooler, the experimental loop system, and the detailed experimental procedure, is described as follows. In Section 2.1, we describe the configuration of MMCHS with geometric dimensions and a few AM techniques for preventing fabrication failure. In Section 2.2, the assembled test module and components of the flow loop system are introduced to control the operating conditions. In Section 2.3 and Section 2.4, we explain the measurement procedure, data reduction, and test uncertainty through MMCHS and loop system.

2.1. Design and fabrication of 3D metal printed manifold-microchannel heat sink

In this section, we describe the design considerations and fabrication details of the MMCHS microcooler test samples. First, we design a detailed manifold channel structure that can be additively manufactured with structural rigidity and flow uniformity. The overall dimension of the sample is 30 × 15 × 9 mm^3 (L × W × H), making it relatively compact with an active heat transfer area of 10 × 10 mm^2. The manifold consists of six inlet branches and seven outlet branches, as shown in Fig. 1(a). The liquid entering the manifold is distributed evenly to the microchannels by adopting a tapered shape for the manifold. The width of the manifold inlet and outlet is 0.45 mm and 1.25 mm, respectively having an inlet-to-outlet ratio of approximately three. This increases the heat transfer rate by increasing the speed of the fluid entering the channel [61]. The microchannel section comprises a total of 21 channels, with a channel width (W_{ch}) of 0.2 mm and a channel height (H_{ch}) of 2.0 mm. The thickness of the base from the bottom of the heat sink is 1.0 mm, which is sufficient to eliminate leakage from the pores formed

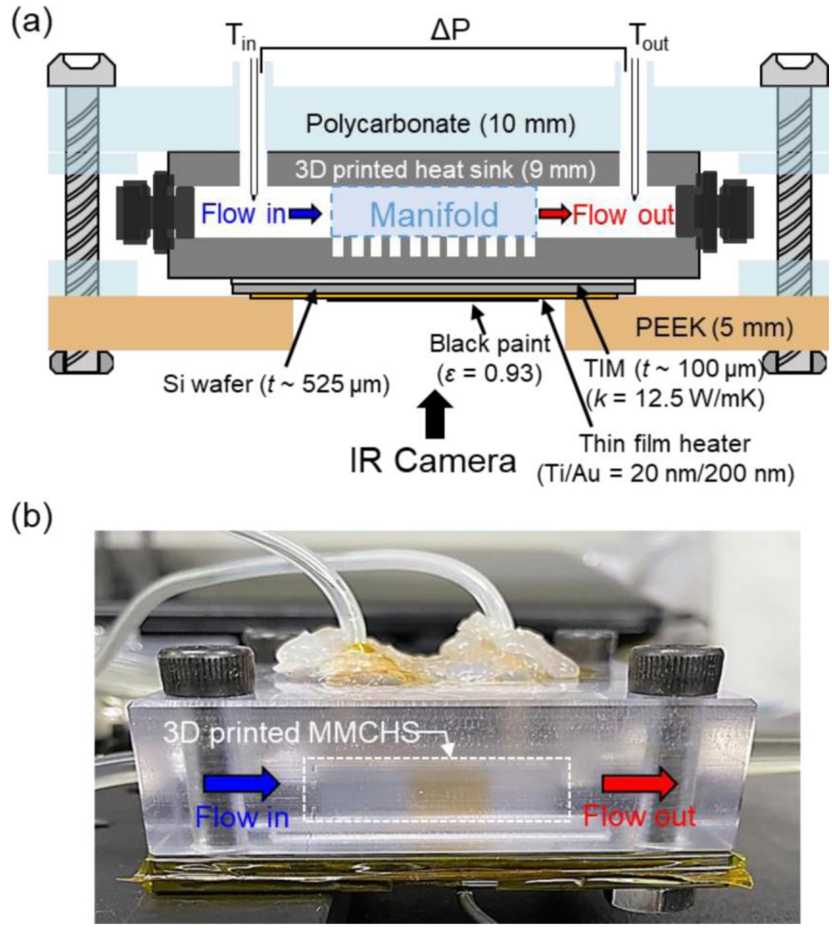

Fig. 2. Assembly of the thermal-fluid test module. (a) Schematic of the cross-section of the test module. (b) Image of the assembled test module. Insulation with a polycarbonate cover around the 3D-printed MMCHS prevents heat losses while providing the simultaneous sensing of fluid temperature and pressure drop.

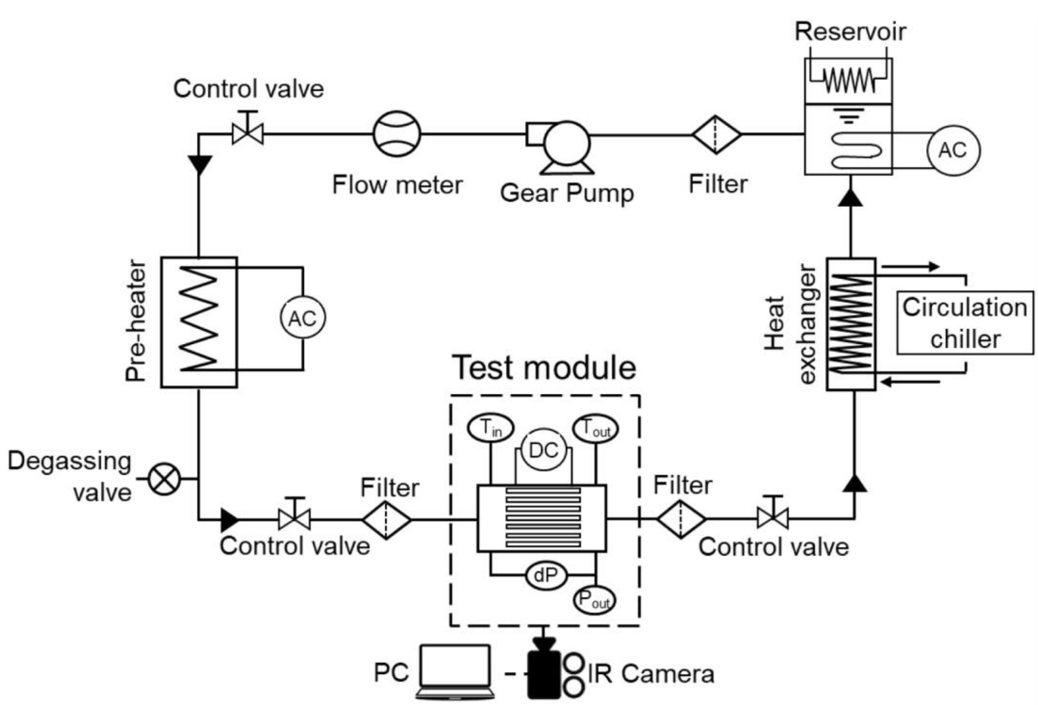

Fig. 3. Schematic overview of the experimental flow loop system. De-ionized water is used as a working fluid. A mass flow rate of 100–400 g/min transported by the micropump is applied to the test module at an inlet temperature of ~20 °C. Joule heating with a thin film heater is applied to the bottom surface of MMCHS, simultaneously observing the surface temperature using the IR camera.

during 3D printing [58]. Adopting a thin wall serves to reduce the pressure drop inside the MMCHS; thus, the channel fin and manifold wall are limited to a thickness of 0.3 mm, which is also the minimum feature size of the AM process [62]. Pillars are fabricated at the entrance and exit plenum of MMCHS as shown in Fig. 1(b) for supporting the structure and preventing overhang while manufacturing the heat sink. The top of the manifold possesses a stable arch design to eliminate structural failure during manufacture. Both top and bottom parts are monolithically fabricated by the LPBF (EOS M290) method using AlSi10Mg powder, which is one of the metal AM technologies. The MMCHS is subsequently heat-treated at 300 °C for 2 h to prevent fluid leakage by filling in pores and to improve overall thermal conductivity ($k = 170$ W/mK) [62].

2.2. Test module & facility of flow loop system

A thermal-fluid test in which the thermal resistance, pressure drop, and coefficient of performance (COP) are measured is conducted to assess the thermal and hydraulic performance of the 3D-printed microcooler. Before the heat transfer evaluation, test rigs including the sample fixer, liquid route housing, and MMCHS heat sink for the test module are assembled. Fig. 2 illustrates each component of the MMCHS test module through the cross-sectional schematic and the image of the assembled test module. For compatibility with the flow loop, the inlet and outlet are fitted with Hy-Lok 3/16" ferrule fittings using silicone paste. A 3 mm hole is drilled into the inlet and outlet plenum to measure the pressure drop using perfluoroalkoxy (PFA) tubes connected to a differential manometer. The inlet and outlet fluid temperatures are measured simultaneously by inserting K-type thermocouples (OMEGA Eng., SCASS-010G-12) with a diameter of 0.01" into the PFA tubes. A thin metal heater (Ti/Au = 20 nm/100 nm) deposited on a silicon wafer through thermal evaporation is attached to the bottom surface of MMCHS using TIM (Thermal Grizzly Kryonaut, $k = 12.5$ W/mK) to create the thermal test vehicle. The 10 × 10 mm^2 of the heated area is carefully aligned with the footprint area of MMCHS. In addition, the polycarbonate (PC) and polyether ether ketone (PEEK) blocks are machined to mount the thermal test vehicle and prevent parasitic heat loss during the experiment. Finally, the entire test setup is assembled by mutually aligning each component. Fig. 3 depicts the schematic of the apparatus of the flow loop system designed to investigate the heat transfer performance and pressure drop characteristics of MMCHS. A magnetically driven gear pump (Micropump GA-T23) is used to drive the working fluid through the test section. A Coriolis mass flow meter (Bronkhorst High-Tech BV, M14) is installed to measure the mass flow rate entering the inlet of the test section. A 50 μm-filter is installed at both ends of the test module to screen impurities during the test. A liquid-to-liquid heat exchanger and a chiller (JEIO TECH Co., Ltd., HH 20) are connected downstream of the sample to remove the heat from the fluid coming out from the outlet. During the experiment, the temperature of the thin-film heater is measured with an IR camera (FLIR A655sc) with a resolution of 640 × 480 pixels. A coating of calibrated high-emissivity black paint (ELE EP-10) is conducted on the heater in order to ensure accurate temperature measurement.

2.3. Operating conditions & experimental procedure

Thermal-fluid testing of the MMCHS is conducted with water as the cooling fluid, operating at a mass flow range of 100–395 g/min, with an inlet absolute pressure in the range of 1.15–1.2 bar. The inlet temperature is maintained in the range of 17.2–20.1 °C. Before testing, water is boiled for 30 min using an immersion heater to degas the coolant and remove any non-condensable gases, which is subsequently cooled down to room temperature before pumping it into the test section. The water temperature at the inlet is controlled by a pre-heater (TECHNE, TE-10D) upstream of the test module. The thin metal heater on the Si wafer, attached to the MMCHS, is powered by a DC power supply (MKPOWER, MK-20015IS). Power is applied to the heater starting from 0 W and the current and voltage are increased by 20 W. To measure the current and voltage applied to the heater, a shunt resistor (Ohmite TGHGCR0500DE) and a voltage divider circuit with a resistance ratio of 40:1 are chosen, and the power is recorded by connecting it to a DAQ analog input module (NI 9220). The water heated from the test module is cooled down in the heat exchanger downstream and returned to the reservoir. When the change in the heater surface temperature remained within ±0.5 °C for 1 min, it is regarded as a steady state and the temperature is recorded using an IR camera. Simultaneously, the fluid temperature of the inlet and outlet, absolute gauge pressure (Trafag AG, ECT 8472), and pressure drop (OMEGA Eng., PX2300-1D) are also logged using a DAQ module integrated into a Labview program.

2.4. Data reduction and uncertainty

The Joule heating, q_{tot}, that powers the metal serpentine heater is computed by multiplying the voltage across the heater, V, by the current flowing through the heater, I. The heat flux is defined as the applied heat divided by the heater area.

$$q''_{tot} = \frac{VI}{A_h} = \frac{q}{A_h} \tag{1}$$

The bottom surface temperature of the MMCHS, T_b, is calculated using Eq. (2), which considers the temperature drop in the Si wafer and TIM.

$$T_b = T_h - \left(\frac{t_{si}}{k_{si}} + \frac{t_{tim}}{k_{tim}}\right) q''_{eff} \tag{2}$$

T_h is the average temperature of the heater surface on the back of Si wafer, and t_{si} and k_{si} are the thickness and thermal conductivity of the Si wafer, respectively, and t_{tim} and k_{tim} are corresponding values of the thermal interface material. The effective heat flux dissipated by the fluid flow in the manifold microchannel, q''_{eff}, is calculated using Eq. (3) which accounts for the conductive heat loss from the total input heat flux.

$$q''_{eff} = q''_{tot} - q''_{loss} = \dot{m} C_p (T_{out} - T_{in}) \tag{3}$$

A major portion of heat loss includes lateral heat dissipation through highly conductive metallic side walls to the inlet and outlet plenums [64], and the remaining portion is transferred to the manifold-microchannel structures and is dissipated by single-phase liquid cooling. The detailed heat flow paths in the microcooler are obtained computationally and are included in Appendix A. Accordingly, the total thermal resistance for different effective heat at each mass flow rate of MMCHS is defined as follows,

$$R_{tot} = \frac{\Delta T}{q_{eff}} = \frac{T_b - T_{in}}{q_{eff}} \tag{4}$$

The coefficient of performance is determined to quantitatively analyze the heat transfer and pressure drop trend of MMCHS, which is defined as the ratio between the amount of heat dissipated and the pumping power required to transport the fluid.

$$COP = \frac{q_{eff}}{q_{pump}} \tag{5}$$

Where q_{eff} is calculated as effective heat flux times the heater area, and q_{pump} is determined by the volumetric flow rate and pressure drop across the heat sink as follows,

$$q_{pump} = \dot{V} \Delta P \tag{6}$$

The accuracy of mass flow rate measurement at the inlet is 0.2%. In addition, the precision of the resistors that receive voltage and current via the voltage divider and shunt resistor is 1% and 0.5%, respectively. Thus, the uncertainty in the measurement of q_{tot} is considered in Eq. (7)

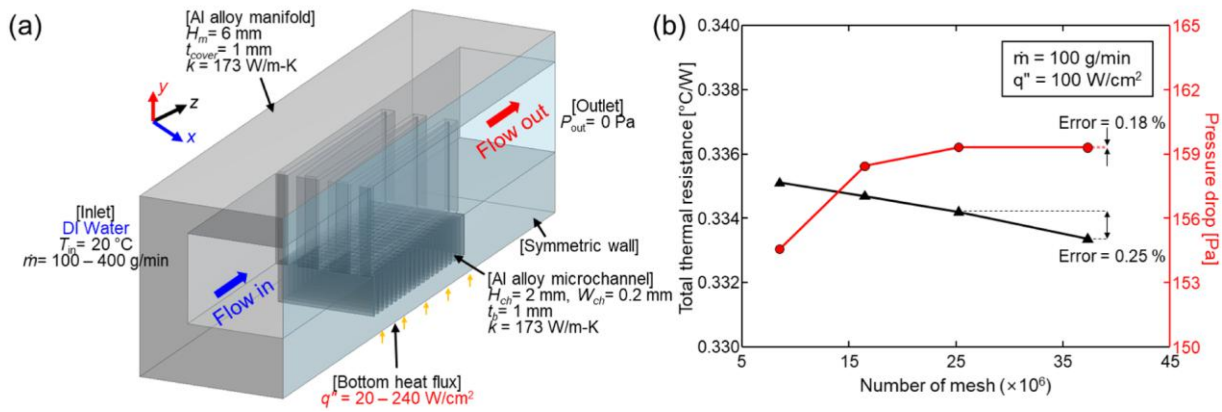

Fig. 4. Computational model and grid independency results. (a) Computational domain for the additively manufactured manifold-microchannel microcooler. (b) The mesh independence test at $T_{in} = 20$ °C, $\dot{m} = 100$ g/min, and q" = 100 W/cm^2. The thermal resistance and pressure drop results are presented by adopting the number of elements from 10^7 to 4×10^7.

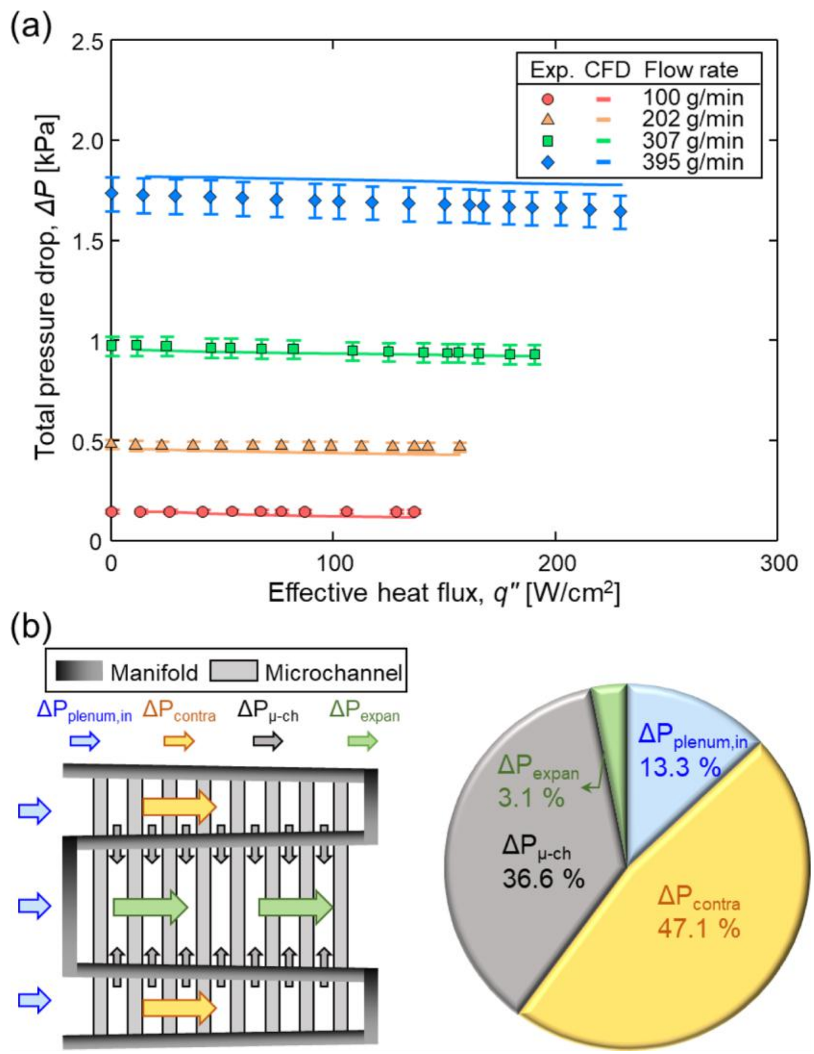

Fig. 5. Comparison of the experimentally measured pressure drop with the numerical results. (a) Single-phase pressure drop in the MMCHS as a function of effective heat flux at $\dot{m}$ = 100–400 g/min. (b) An averaged proportion of pressure drop to total pressure drop for each section of MMCHS. Based on the CFD results, 47.1% of the total pressure drop occurs in the converged manifold structure (ΔP_{contra}), and 36.6% of the total pressure drop is contributed to the microchannels ($\Delta P_{\mu\text{-}ch}$).

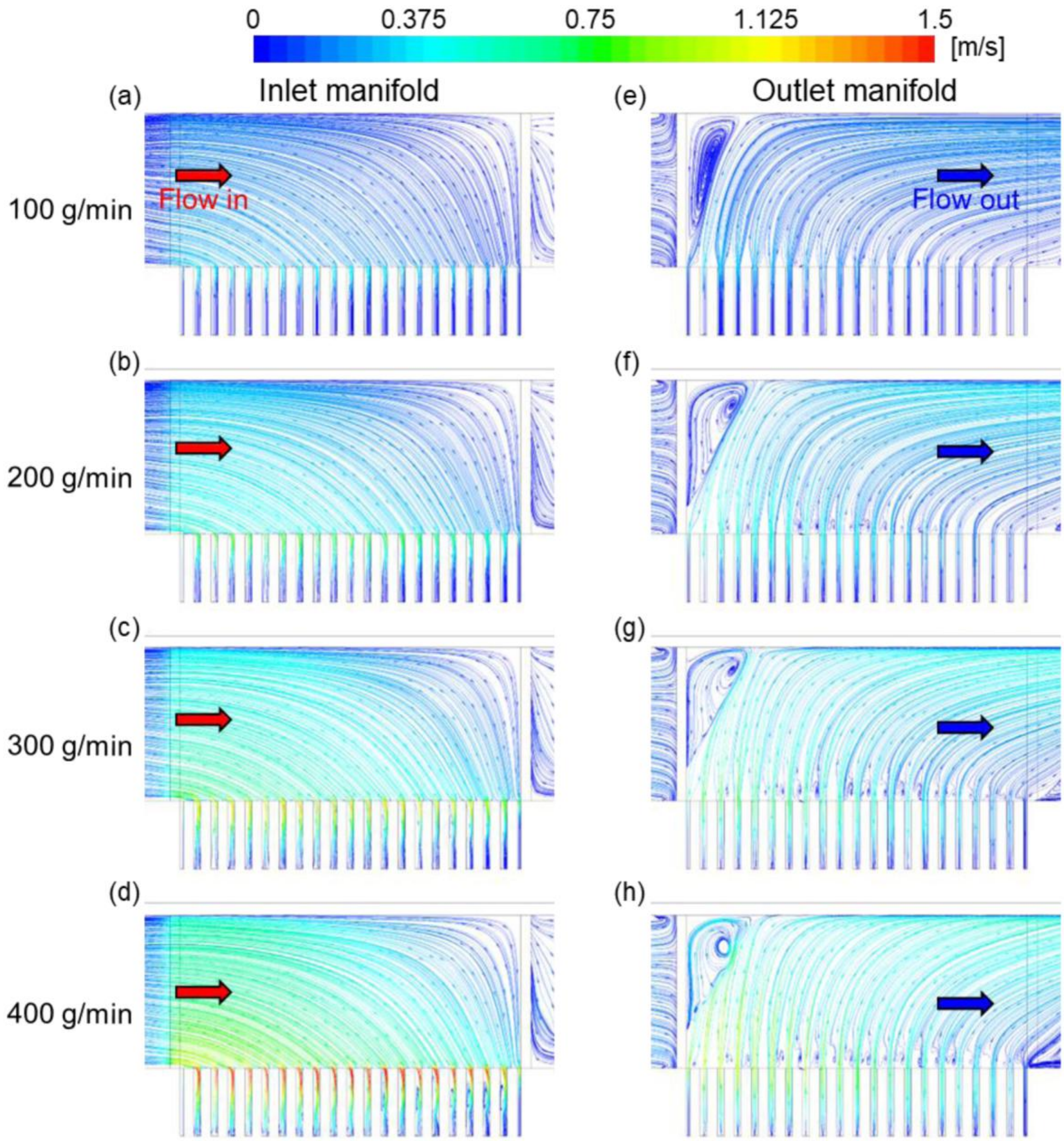

Fig. 6. Streamline computations in the MMCHS. Cross-sectional streamlines at the center of the manifold inlet (a–d) and manifold outlet (e–h). At the high flow rate of 400 g/min in d, the flow separation is intensified inside the channel and makes the vortices. In addition, the sudden opening from the channel to the outlet manifold causes the vortices, resulting in a lower channel velocity, as shown in h.

and calculated to be ±1.4%.

$$\left(\frac{U_{q_{tot}}}{VI}\right)^2 = \left(\frac{U_V}{V}\right)^2 + \left(\frac{U_I}{I}\right)^2 \quad (7)$$

The absolute gauge pressure and differential pressure transducer readings from inside the sample have respective precisions of 0.5 and 0.25%. The accuracy of the inlet and outlet thermocouples is ±1.1°C, and the temperature of the heated surface measured from the IR thermometer has an accuracy of ±2 °C. Moreover, the TIM thickness is measured by a micrometer, which has a 0.01 mm accuracy. Therefore, based on Eq. 8, the total thermal resistance in the MMCHS exhibits uncertainties of 2.1–17.9% [63].

$$\left(\frac{U_{R_{tot}}}{R_{tot}}\right)^2 = \left(\frac{U_{T_{h,avg}}}{\Delta T_{lm}}\right)^2 + \left(\frac{U_{T_{f,in}}}{\Delta T_{lm}}\right)^2 + \left(\frac{U_{T_{f,out}}}{\Delta T_{lm}}\right)^2 + \left(\frac{U_{q''_{tot}}}{q''_{tot}}\right)^2 + \left(\frac{U_{t_{tim}}}{t_{tim}}\right)^2 \quad (8)$$

3. Computational modeling

Before experimentally evaluating the thermal and hydraulic performance of the MMCHS at a high heat flux, a 3D conjugate heat transfer is performed with a symmetric design. From a holistic standpoint, we address the impact of operational conditions on the relationship between the detailed fluid flow and heat transfer performance inside the MMCHS. Therefore, the analysis of the total pressure drop and uniformity of the channel velocity in the MMCHS at four mass flow rates is summarized through numerical modeling.

3.1. CFD simulation domains and governing equations

In this section, the simulation domain and boundary conditions of the MMCHS are explained line-by-line. Furthermore, governing equations with adequate discretization methods are used to solve the thermofluidic behavior. To compute the 3D computational domain used in

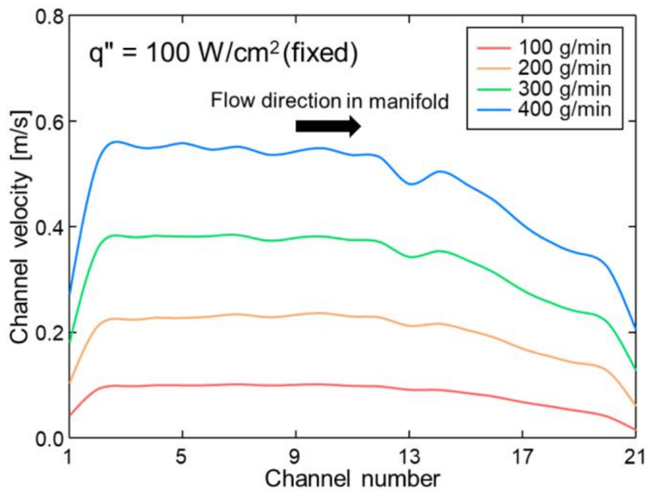

Fig. 7. Variations of the channel velocities at the center of the inlet manifold. The velocity at each channel has a uniform value in channels 1–12. The velocity in channels 13–21 gradually decreases due to the narrower manifold path and flow resistance.

the simulation of the MMCHS, we employ symmetric modeling that can reduce the CFD domain size, thereby minimizing the computational costs, as shown in Fig. 4(a). The solid domain in the model is monolithic and hence was made of a single material, Al alloy ($k = 173$ W/mK). The fluid domain is DI water with an inlet and outlet on either end of the CFD domain. Four mass flow rates in the range of 100–400 g/min, similar to those in the experiment, are applied at the inlet at a constant temperature of 20 °C, and a pressure outlet boundary condition with a gauge pressure of 0 Pa is applied at the outlet. The constant heat flux boundary condition, identical to the experimental condition, is applied at the base of MMCHS. A convective heat transfer rate of 10 W/m^2-K is applied to the outer walls of the CFD domain to simulate the experimental environment. The symmetric wall condition is applied to the sidewall of the MMCHS, and an insulation condition is applied to its remaining surfaces. Since the difference in the measured pressure drop values between the rough and smooth surfaces is within 4% as shown in Appendix B, a smooth surface is applied to the fluid-solid interface even if it has a roughness in the fabricated MMCHS. Pressure-velocity coupling is implemented using the Semi-Implicit Method for Pressure-Linked Equations (SIMPLE) algorithm, and the least squares cell-based scheme and second order scheme are adopted for gradient and pressure discretization, respectively. The second-order upwind scheme is applied to the momentum and energy terms. A shear stress transport (SST) k–ω turbulence model is applied to account for turbulence as the fluid moves in and out of the manifold and microchannel boundary [65–68]. It has been reported that k–ω turbulence model or the SST turbulence models perform better in such low Reynolds number flows as compared to the ε-equation based k–ε model that is designed typically for high Reynolds number flows [69,70]. A commercial code, ANSYS Fluent 19.2, is used for CFD simulation, and the governing equations used for continuity, momentum, energy, k, and ω used are as follows.

Continuity equation:

$$\frac{\partial}{\partial x_i}(\rho u_i) = 0, \tag{9}$$

Momentum equation:

$$\frac{\partial}{\partial x_j}(\rho u_i u_j) = \frac{\partial p}{\partial x_i} + \frac{\partial}{\partial x_j}\left(\mu \frac{\partial u_i}{\partial x_j} - \rho \overline{u'_i u'_j}\right), \tag{10}$$

Energy equation:

$$\frac{\partial}{\partial x_i}(\rho u_i T) = \frac{\partial}{\partial x_i}\left(\frac{\mu}{\mathrm{Pr}} \frac{\partial T}{\partial x_i}\right), \tag{11}$$

k equation:

$$\frac{\partial}{\partial x_i}(\rho k u_i) = \frac{\partial}{\partial x_j}\left(\Gamma_k \frac{\partial k}{\partial x_j}\right) + G_k - Y_k, \tag{12}$$

ω equation:

$$\frac{\partial}{\partial x_i}(\rho \omega u_i) = \frac{\partial}{\partial x_j}\left(\Gamma_\omega \frac{\partial \omega}{\partial x_j}\right) + G_\omega - Y_\omega, \tag{13}$$

where u_i is the velocity vector in the x, y, and z directions, and ρ, μ, C_p, and k are the density, dynamic viscosity, specific heat, and thermal conductivity, respectively. Γ_k and Γ_ω are the effective diffusion terms of k and ω, and G and Y are the generation and dissipation terms, respectively. The mesh comprises structured conformal hexahedral elements in all domains, and a mesh independence test is performed using the number of meshes, as shown in Fig. 4(b). At a mass flow rate of 100 g/min, the pressure drop reaches an asymptotic line when the number of meshes used is 37 million, and its difference from the pressure drop corresponding to 25 million meshes is 0.18%. Although thermal resistance changes almost linearly with mesh size, it exhibits only a marginal difference of 0.25% between the finest mesh size and the preceding one. In this CFD simulation, all cases are calculated using the smallest mesh

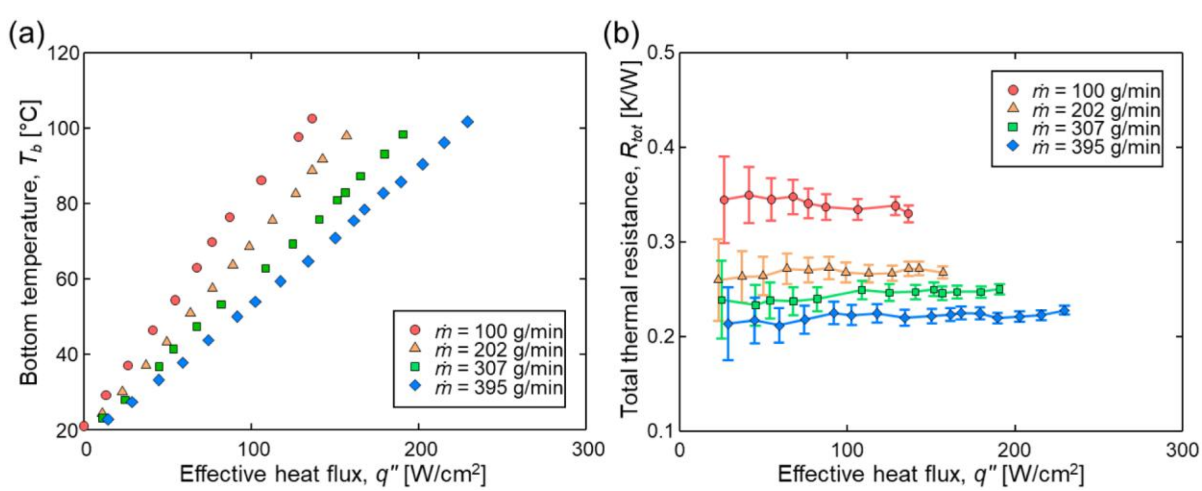

Fig. 8. Thermal performance evaluation of the MMCHS. The experimental results for (a) the averaged bottom surface temperature and (b) the corresponding total thermal resistance of MMCHS at a given heat flux and the mass flow rate of 100–400 g/min. The value of $\Delta T_b/\Delta q''$ decreases from 0.60 to 0.37 and the total thermal resistance decreases from 0.35 to 0.21 K/W.

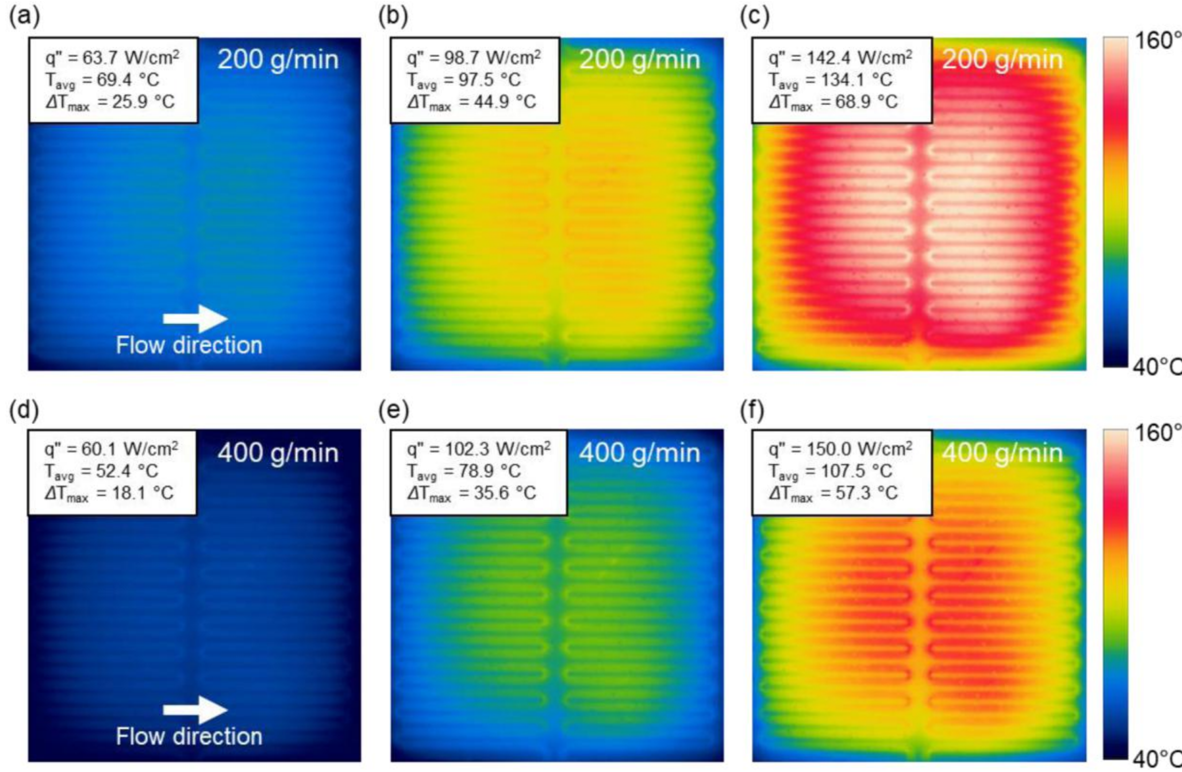

Fig. 9. Temperature rise on the heated surface obtained by an infrared camera. Infrared measurements of heated surface for two different mass flow rates of (a–c) 200 g/min and (d–f) 400 g/min. At a heat flux of approximately 150 W/cm^2 in c and f, the hot spot temperature is highlighted on the right side of the heater due to the reduced channel velocity.

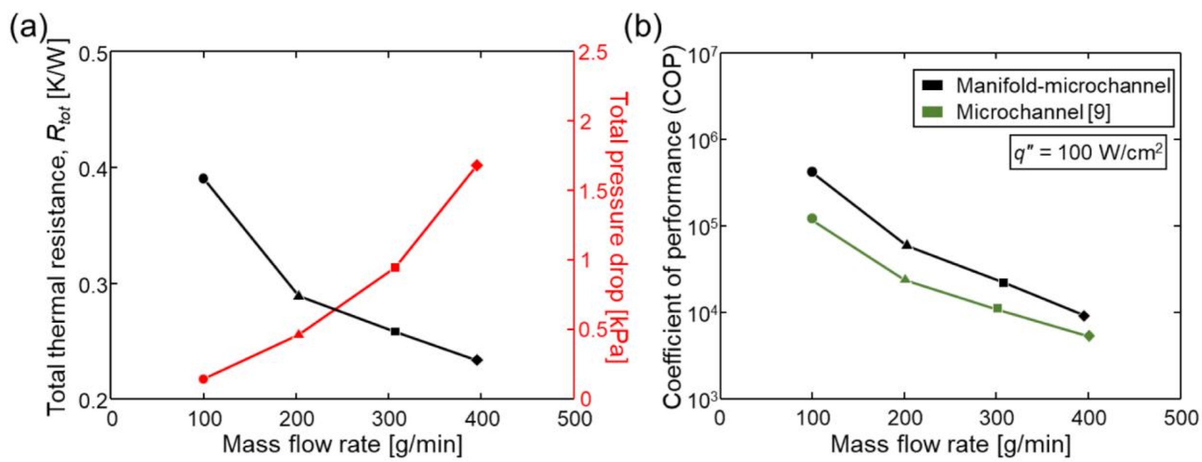

Fig. 10. Thermal-hydraulic analysis on MMCHS. (a) Trends of total thermal resistance (black) and pressure drop (red) at the mass flow rate of 100–400 g/min and the constant heat flux of q" = 100 W/cm^2. (b) The coefficient of performance of MMCHS is 1.7–3.6 times higher than that of MCHS at all flow rates due to the shorter flow channel formed by the integration of the manifold structure to traditional MCHS, which reduces pumping power.

size.

4. Results and discussion

The following sections present the characterization of the heat transfer and hydraulic performance parameters of the MMCHS, such as heat fluxes and mass flow rates. In addition, the detailed flow field inside the MMCHS, which is difficult to obtain experimentally, is analyzed using CFD simulations and compared with the experimental results. In Section 4.1, an analysis of the pressure drop on the MMCHS is described using experimental and numerical data. Furthermore, numerical analysis of the partial pressure drop provides insight into the hydrothermal enhancement through the geometrical effect. In Section 4.2, the heated surface temperature and total thermal resistance of the MMCHS are investigated in terms of the hydraulic characteristics described in Section 4.1. In Section 4.3, the pumping power and coefficient of performance of the MMCHS are assessed to determine its thermal efficiency and benchmarked with the conventional microchannel heat sink.

4.1. Pressure drop and flow field results

In a microfluidic cooling system, the pressure drop is indicated as a

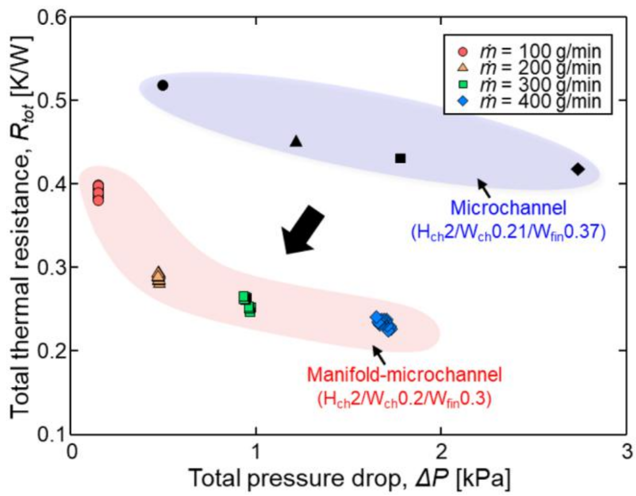

Fig. 11. A benchmark comparison of the experimentally determined thermal-hydraulic performance of MMCHS with conventional microchannel. The black markers are experimental results of the microchannel heat sink from Ref. [9]. Both thermal resistance and pressure drop are reduced compared to the conventional microchannel due to the advantages of integration of the manifold structure with the microchannel.

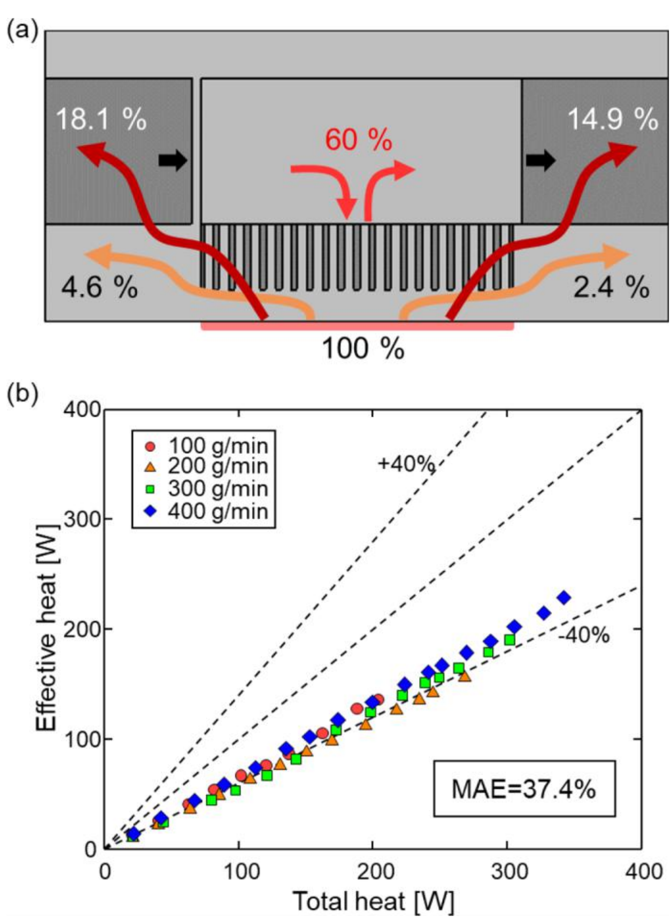

Fig. A.1. Analysis of the portion of dissipated heat on the MMCHS. (a) An averaged ratio of the dissipated heat amount in the AM MMCHS. Conductive base thickness and monolithic AM design dissipate ~40% of total heat. It is validated with (b) the experimental comparison of effective heat versus total heat.

factor that impedes energy efficiency. Thus, the experimental pressure drop in the MMCHS is measured at the different mass flow rates and heat fluxes, and the numerical results validate the fluid flow in the MMCHS. The ratio of the total pressure drop for the design improvement of the MMCHS is also analyzed in detail in terms of efficient fluidic behavior.

First, the mass flow rate is controlled in 100 g/min increments from 100 to 400 g/min to characterize the pressure drop across the MMCHS. Fig. 5(a) depicts the experimentally determined pressure drop as a function of heat flux. As expected, the pressure drop for the same mass flow rate is almost constant or decreases monotonically with increasing heat flux since the fluid viscosity decreases with increasing temperature. As the mass flow rate increases from 100 to 400 g/min, the pressure drop increases significantly from a minimum of 0.15 kPa to a maximum of 1.7 kPa. The pressure drop across the MMCHS, determined by the CFD simulation for the same geometric morphology and operating conditions as in the experiment, is represented by solid lines in Fig. 5(a). It can be observed that the numerically obtained total pressure drop agrees well with the experimental data as the overall mean absolute error is merely 5.2%. Fig. 5(b) shows the proportion of pressure drop across each section as the fluid moves from the inlet of MMCHS through the plenum, manifold inlet, microchannel, and to the outlet through CFD analysis. ΔP_{contra}, which has the largest proportion of total pressure drop, accounts for 47.1% of the total pressure drop. This is the pressure drop in the region of the manifold inlet with a contraction between the manifold and microchannel. At 36.6%, the second largest is $\Delta P_{\mu\text{-ch}}$, which is the pressure drop at the entrance of the microchannel and is because of the small hydraulic diameter of the microchannels. $\Delta P_{\text{plenum,in}}$, the pressure drop generated across the inlet plenum and up to the manifold is caused by the stagnation effect because of the manifold wall and the decrease in the cross-sectional area where the fluid enters, resulting in approximately 13.3% of the total pressure drop. Finally, ΔP_{expan} is the pressure drop at the region between the microchannel and the outlet. The flow in this region is subjected to merely 3.1% of the total pressure drop owing to the wide hydraulic diameter of the diverged manifold outlet. In conclusion, in conventionally shaped MMCHSs pressure drop primarily occurs within the manifold inlet and the microchannel. In the future, finer 3D printing processes can be used to improve hydraulic performance by reducing pressure drop because of the sudden contractions within the manifold and microchannels.

In order to figure out the fluidic behavior inside MMCHS, the streamlines at the inlet and outlet of MMCHS and the mean fluid velocity of each channel are investigated. Fig. 6 illustrates the cross-sectional streamlines at the central surface of the inlet and outlet manifolds. As shown in Fig. 6(a)–(d), vortices are generated within the microchannels near the outlet manifold when the fluid collides and bounces off the microchannel wall. This is exacerbated in the case of higher velocity fluid entering the microchannel from the manifold, resulting in less fluid being introduced into the channels located far from the inlet of the manifold. As shown in Fig. 6(e)–(h), a large flow circulation exists near the upper left corner of the manifold outlet because of the sudden changes in the flow direction. Furthermore, several small vortices are developed at the microchannel exit because of the sudden expansion when the fluid exits the microchannel into the manifold. Larger vortices are observed with increasing fluid velocities. Overall, the vortices generated in the microchannel and the space between the microchannel and the manifold increase the local pressure drop and decrease the flow rate, resulting in non-uniform flow distribution.

The uniform distribution of channel velocity also helps to understand a uniform and stable chip temperature. Thus, we also investigate the average velocity of each microchannel in the central section of the manifold inlet from the CFD results as shown in Fig. 7. When fluid enters the channels, the flow velocity is relatively lower in the first channel because of vena contracta caused by a sudden contraction but flows at an almost constant velocity from the second to the middle channel. The flow velocity starts to decrease from the middle to the last channel because of the vortices generated inside and above the microchannels.

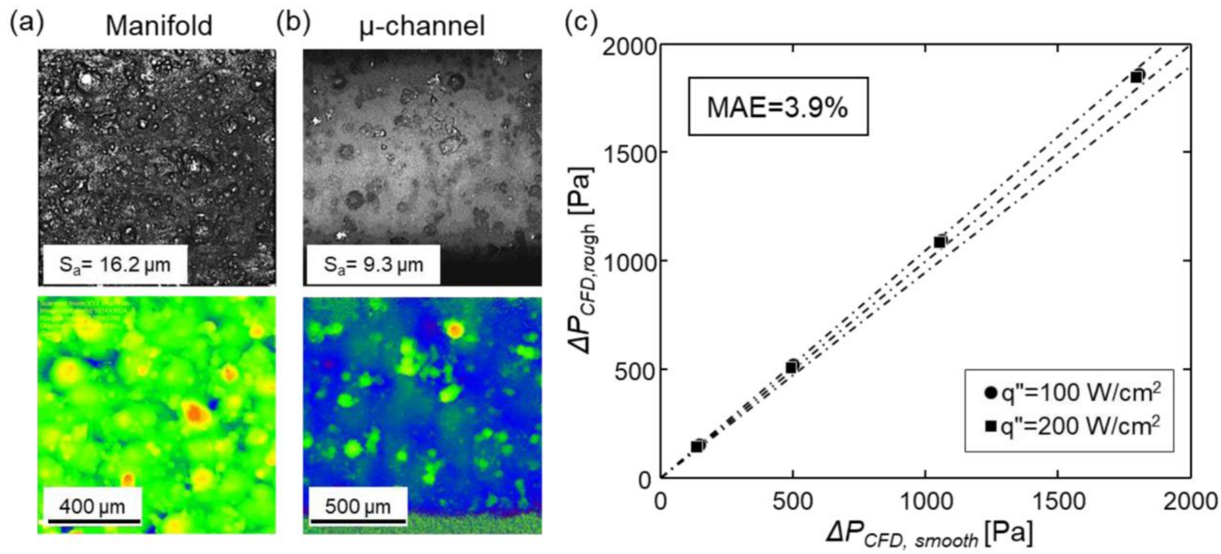

Fig. B.1. Numerical comparison of pressure drop depending on surface roughness. Confocal images of (a) manifold wall and (b) microchannel wall. (c) The mean absolute error for the pressure drop between a smooth wall and a rough wall with a flow rate of 100–400 g/min indicates ~4%, barely any different owing to low velocity.

More detailed streamlines and temperature contours along with the microchannel length are described in Appendix C. Thus, as described in Fig. 6, the strength of the vortices generated in the microchannel increases along with the mass flow rate. This cause augments the vortex generation area, thereby reducing the fluid flow into the channel.

4.2. Temperature and thermal resistance results

A report on the heated surface temperature and total thermal resistance is presented to assess the thermal performance of the MMCHS by measuring the bottom temperature and resulting thermal resistance. Based on the results of the pressure drop and distribution of the fluid velocity inside the channels in Section 4.1, the temperature distribution of the hotspot and the total thermal resistance can be inferred and evaluated in terms of effective heat transfer. The experimental values of the average temperature of the bottom surface of the MMCHS corresponding to various effective heat fluxes for each mass flow rate are shown in Fig. 8(a). For the same flow rate, the bottom surface temperature increases almost linearly as the heat flux increases. And as the flow rate increases from 100 to 400 g/min, the value of $\Delta T_b/\Delta q''$ decreases from 0.60 to 0.37. In addition, the applied effective heat flux increases by 69.7% from a minimum of 132–224 W/cm^2 when the bottom surface temperature reaches 100 °C. This enhancement is attributed to the increase in the flow rate in the microchannel and the increase in the convective heat transfer rate because of the mixing effect of the vortex in the channel, as shown in Fig. 6. Fig. 8(b) presents the experimentally calculated total thermal resistance for different effective heat fluxes at each mass flow rate of MMCHS. At a mass flow rate of 100 g/min, the total thermal resistance varies because of the large uncertainty in flow. However, the trend of the result can be expressed as almost constant. At the same flow rate, the total thermal resistance remains almost constant within the range of 0.21–0.35 K/W as the heat flux increases. Moreover, the thermal resistance decreases by 25.9% when the flow rate increases from 100 to 200 g/min because of the increase in convective heat transfer in the microchannel. However, since the conductive thermal resistance is almost constant while the convective thermal resistance proportionally decreases as the flow rate increases beyond 300 g/min, the total thermal resistance is reduced by approximately 10%.

Similarly, the uniformity of the surface temperature is investigated based on the distribution of the fluid velocity at the microchannel, as discussed in Section 4.1. We may infer the temperature distribution of the heated surface indirectly by visually observing the IR thermal mapping at different heat fluxes, as shown in Fig. 9. The fluid flow at the inlet of the manifold proceeds from left to right, and the flow in the microchannel proceeds in a vertical direction. As the heat flux increases to approximately 50 W/cm^2 for each flow rate, the heater temperature increases monotonically in single-phase cooling. Furthermore, the hot spot shifts marginally to the right of the center because of non-uniform flow velocity (i.e., because of the low flow at the manifold outlet side) in the microchannel. The temperature drop appears at the edge of the heater because of the lateral heat spreading of MMCHS. In addition, as the flow rate increases from 200 to 400 g/min, the average temperature and maximum temperature difference of the heater for the same heat flux decrease by 17.0–26.6 °C and 7.8–11.6 °C, respectively.

4.3. Evaluation of thermal and hydraulic performance

In this section, the thermal and hydraulic performances of the MMCHS are comprehensively analyzed to determine the suitable operating conditions that maximize the heat transfer rate while minimizing the pressure drop. Furthermore, the coefficient of performance that determines the cooling efficiency of the MMCHS is compared with that of the microchannel (MCHS) as a reference index. First, the average total thermal resistance and pressure drop are characterized by the mass flow rate, as shown in Fig. 10(a). Total thermal resistance is drastically reduced, showing a decrease of 40% to 0.21 K/W at a mass flow rate of 400 g/min, compared to 0.35 K/W at a mass flow rate of 100 g/min. In contrast, the relatively low-pressure drop of 0.15 kPa for the mass flow rate of 100 g/min exponentially increases to 1.7 kPa for the mass flow rate of 400 g/min, which is approximately an 11-fold increase. This clearly indicates a tradeoff between thermal and hydraulic performance in MMCHS. Fig. 10(b) presents the comparison of COPs between MMCHS and conventional microchannel heat sink as a function of mass flow rate for dissipating the same effective heat flux of 100 W/cm^2. The geometry of the microchannel is dimensionally similar to the structure fabricated in this study with $W_{ch} = 0.21$ mm, $W_{fin} = 0.37$ mm, and $H_{ch} =$ 2 mm. The COP is calculated for the same mass flow rates used in this study [9]. As the flow rate increases, the COP tends to decrease because of the increasing pressure drop for the same heat flux. MMCHS exhibits a COP that is 1.7–3.6 times that of MCHS at all flow rates. This is because the pumping power decreases owing to the shortened flow path created by adding the manifold structure.

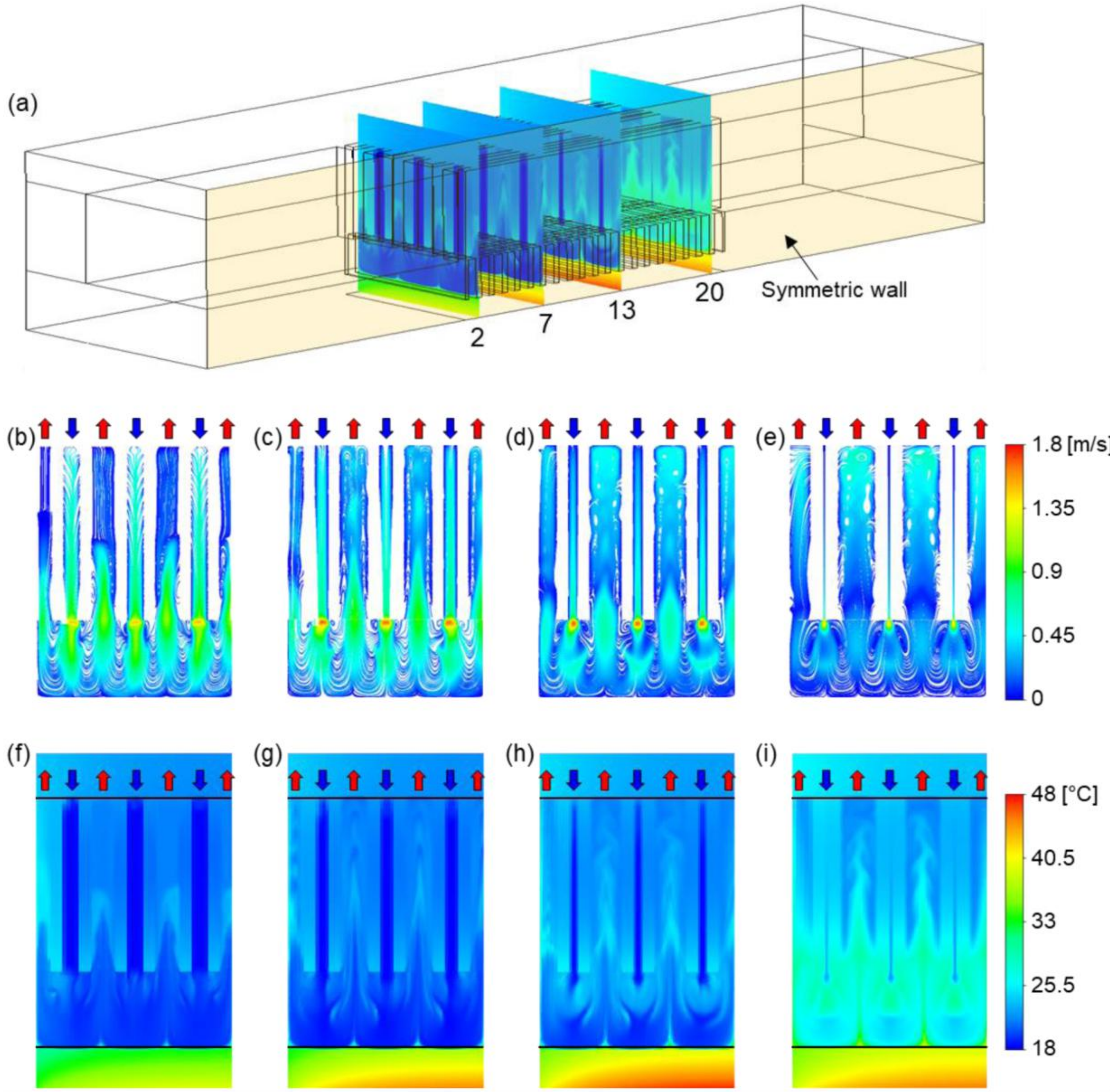

Fig. C.1. Streamline and temperature cross-sectional contours of MMCHS. (a) MMCHS modeling and the channel number of each contour. (b–e) streamlines for channel numbers 2, 7, 13, and 20, respectively, and (f–i) the corresponding temperature contours at a flow rate of 400 g/min and effective heat flux of 100 W/cm^2.

We also benchmark the thermal performance of our additive-manufactured microcooler with the conventional microchannel to investigate the effort of manifold structure. Pure aluminum microchannel is chosen as a baseline, and the total thermal resistance of each microcooler is expressed as a function of pressure drop for each flow rate as shown in Fig. 11. The measured data points show the average total thermal resistance and pressure drop obtained during the thermal test. The black symbols represent the results of the conventional microchannel, and the experimental results for the same microchannel shape are specified for comparison with the experimental result of MMCHS [9]. For the same heat flux of 100 W/cm^2, the pressure drop of MMCHS is at least 37.9% lower than that of MCHS, with the difference increasing to 70.2%. In addition, the total thermal resistance also decreases by at least 24.2% with the difference increasing to 44.0% compared to the microchannel heat sink, indicating improved heat transfer performance. This thermal fluid performance improvement can be attributed to various complex reasons as follows: 1) lowered pressure drop because of the short flow path inside the channel owing to the inclusion of the manifold structure, 2) heat spreading through an all-metallic AM heat sink as well as microfluidic performance, 3) reduced thermal boundary layer obtained using the jet impingement of the 3D manifold.

5. Conclusions

In this study, a manifold microchannel heat sink (MMCHS) with tapered manifold inlets and outlets is designed and fabricated using a metal additive manufacturing process called laser powder bed fusion (LPDF). AlSi10Mg powder is used to fabricate this aluminum-alloy-based heat sink, which is subsequently heat-treated to reduce porosity. This improves the thermal conductivity of the heat sink and reduces fluid leakage. Design considerations, including the use of an arch-shaped top cover and micropillars in the inlet and outlet plenums, are implemented to improve the manufacturability of the heat sink.

Thermal-fluid characterization of the fabricated heat sink at various heat fluxes and water flow rates is conducted through a combination of 3D conjugate heat transfer simulations and experimental testing. As observed experimentally and computationally, the pressure drop across the MMCHS increases from 0.15 to 1.7 kPa as the flow rate increases from 100 g/min to approximately 400 g/min. Up to 47.1% of the total pressure drop for all the flow rates is observed at the manifold inlet region, where the flow changes direction to enter the microchannel and experiences a sudden contraction in the flow cross-section. The pressure drop across the microchannel section results in 36.6% of the total pressure drop. Hence, it is important to optimize these geometries to reduce the overall pressure drop of the heat sink.

While the pressure drop increases with an increase in the mass flow rate, there is a 24.9% drop in the thermal resistance when the flow rate increases from 100 to 200 g/min. However, there is only a 10% drop when the flow rate increased from 200 to 300 g/min. This is due to the limitation of a fixed conductive resistance in the heat sink. A significantly lower thermal resistance of 0.21 K/W is observed for a mass flow rate of 400 g/min. This results in a dissipation of 224 W/cm^2 for a heater average temperature of 100 °C compared to only 132 W/cm^2 at 100 g/min for the same heater temperature.

IR imaging of the heat source on the back side of the heatsink shows a monotonic increase in the maximum temperature with heat flux for a particular mass flow rate. However, for a fixed heat flux, a higher flow rate shows a smaller average temperature, as noted previously, and also a spatially smaller temperature range. However, as the heat flux increased, the hotspot location shifted toward the outlet manifold. This is caused by the non-uniform flow in the microchannels. The CFD simulations show significant vortex generation inside the microchannels owing to the jet-like impingement of the fluid inside the microchannel. This results in an uneven flow distribution in the microchannels as the flow velocity increases up to the second channel, and a constant velocity is maintained in the middle channels. After the velocity decreases, a reduction in fluid flow is observed in the latter microchannels. Hence, the hotspot shifts towards the manifold outlet. Significant vortex formation is also observed at the microchannel and manifold outlets. This formation intensifies with increasing flow rate. This vortex generation leads to an increased pressure drop in the heat sink and an uneven flow distribution.

As described previously, the mass flow rate has an inverted relationship with the thermal resistance and pressure drop. For an increased mass flow rate of 400 g/min, there is a 40% drop in thermal resistance to 0.21 K/W from 0.35 K/W for 100 g/min. However, the pressure drop increases by 11 times for the same flow rate. Hence, an optimal operating condition must be determined to achieve a high coefficient of performance.

In summary, the thermal-hydraulic characteristics of a manifold heat sink are presented, and the effects of several geometric parameters are discussed to improve the performance. With the potential of metal additive manufacturing, complex structural shapes can be fabricated to prevent vortices and ensure an even flow distribution to dissipate high heat fluxes at low-pressure drops. In addition, the additive manufacturing process can be leveraged to create porous manifold-microchannel heat sinks to promote flow boiling and dissipate even higher heat fluxes.

CRediT authorship contribution statement

Daeyoung Kong: Data curation, Formal analysis, Investigation, Methodology, Writing – original draft. **Euibeen Jung:** Investigation, Writing – review & editing. **Yunseo Kim:** Data curation, Formal analysis, Investigation. **Vivek Vardhan Manepalli:** Data curation, Formal analysis. **Kyupaeck Jeff Rah:** Supervision. **Han Sang Kim:** Supervision. **Yongtaek Hong:** Supervision. **Hyoung Gil Choi:** Supervision. **Damena Agonafer:** Writing – review & editing. **Hyoungsoon Lee:** Supervision, Writing – review & editing.

Declaration of Competing Interest

The authors declare that they have no known competing financial interests or personal relationships that could have appeared to influence the work reported in this paper.

Data availability

Data will be made available on request.

Acknowledgments

This research was supported by Global Technology Center, Samsung Electronics Co., Ltd., the Industrial Technology Innovation Program (No. 20007058, Development of safe and comfortable human augmentation hybrid robot suit) funded by the Ministry of Trade, Industry & Energy (MOTIE, Korea), and the Chung-Ang University Graduate Research Scholarship in 2020.

Appendix A. Ratio of convective cooling compared to total heat

In order to investigate the heat losses to the conductive side wall and fluid, the ratio of dissipated heat was calculated in terms of total heat as shown in Fig. A.1(a). CFD results were utilized to quantitatively analyze the heat amount due to the ease of separation of each section. Transferred heat was separated into (i) convection in manifold microchannel, (ii) lateral conduction to AlSi10Mg, (iii) convection-conduction in the side plenums. As expected, most of the heat was mainly dissipated in the microchannels due to high fluid velocity and strong convection with 60% of total heat. However, heat losses occupied 40% due to the conductive metal heating to the side substrate and convection at the inlet/outlet plenums. This heat loss was reflected in the experimental results as well. We compared the total heat ($q_{tot} = V \times I$) versus effective heat ($q_{eff} = \dot{m} \times C_p \times \Delta T$) in the microchannels at overall flow rates as shown in Fig. A.1(b). The mean absolute error of the results meant the average heat loss of total heat and showed a difference of 37.4% which is similar to the CFD analysis. This side heat dissipation in AM-based micro-cooler could be an incidental effect in the high heat flux cooling and should be treated carefully in calculating the thermal resistance or heat transfer coefficient in AM micro-coolers in the future.

Appendix B. Roughness effect on hydraulic performance

The AM fabricated manifold and microchannel walls were visually inspected to analyze the roughness as shown in Fig. B.1(a) and (b). Two surfaces were scanned by 3D confocal microscopy (OLS4100-SWF, Olympus Co., Ltd., Japan), and calculated the average surface roughness. In the microchannel, the surface showed a relatively smooth surface (S_a = 9.3 μm) compared to the manifold surface (S_a = 16.2 μm) since the base substrate of the microchannel was stable as a bulk AlSi10Mg. However, since the manifold was fabricated on the top surface of the microchannel, the manifold floated unstably and showed rough surfaces. Although two surfaces had a large roughness, it was not found the fluid permeable porous walls owing to the heat treatment. It closed the pores and prevented the leakages from penetrating the liquid through the walls. We also compared the CFD results about pressure drop on the smooth and rough surface in the MMCHS as shown in Fig. B.1(c). Averaged roughness height of 12.7 μm and a roughness constant of 0.5 was applied to the CFD calculation. Due to the roughness effect, the total pressure drop of rough surfaces showed slightly higher values than that of smooth surfaces, but the difference was 3.9%, which was not nearly changed in the laminar flow.

Appendix C. Hydrothermal behavior of each channel

To confirm the hydraulic phenomenon in the MMCHS, we further analyzed the streamlines and temperature contours along with the microchannel length as shown in Fig. C.1. The fluid velocity passing through the inlet manifold slightly increased by the surrounding vortices as shown in Fig. C.1(b)–(e). However, we could confirm that the enlarged vortices near the channel and the unstable velocity in the outlet manifold interrupted the fluid motion from channel number 13 and suddenly started the fluid velocity decreasing in Fig. C.1(d), (e). According to the velocity trends, Fig. C.1(f)–(i) showed the temperature of the base substrate of each channel number. In channel number 13 in Fig. C.1(h), the high base temperature was obtained since the fluid flow outcoming the manifold did not reach the bottom surface of the channel and weakened the convective heat transfer. Fig. C.1(i) showed that even though it has the lowest velocity in channel number 20, the base temperature was lower than channel number 13 due to the side wall conduction effect at the outlet plenum as noted in Appendix A.

References

[1] Mudawar I. Recent advances in high-flux, two-phase thermal management. J Therm Sci Eng Appl 2013;5:021012.
[2] Andresen M, Liserre M. Impact of active thermal management on power electronics design. Microelectron Reliab 2014;54:1935–9.
[3] Garimella SV, Persoons T, Weibel JA, Gektin V. Electronics thermal management in information and communications technologies: challenges and future directions. IEEE Trans Compon Packag Manuf Technol 2017;7:1191–205.
[4] Anandan S, Ramalingam V. Thermal management of electronics: a review of literature. Therm Sci 2008;12:5–26.
[5] Palko JW, Lee H, Zhang C, Dusseault TJ, Maitra T, Won Y, Agonafer DD, Moss J, Houshmand F, Rong G, Wilbur JD, Rockosi D, Mykyta I, Resler D, Altman D, Asheghi M, Santiago JG, Goodson KE. Extreme two-phase cooling from laser-etched diamond and conformal, template-fabricated microporous copper. Adv Funct Mater 2017;27:1703265.
[6] Alihosseini Y, Targhi MZ, Heyhat MM, Ghorbani N. Effect of a micro heat sink geometric design on thermo-hydraulic performance: a review. Appl Therm Eng 2020;170:114974.
[7] Fedorov AG, Viskanta R. Three-dimensional conjugate heat transfer in the microchannel heat sink for electronic packaging. Int J Heat Mass Transf 2000;43: 399–415.
[8] Qu W, Mudawar I. Experimental and numerical study of pressure drop and heat transfer in a single-phase micro-channel heat sink. Int J Heat Mass Transf 2002;45: 2549–65.
[9] Zhang HY, Pinjala D, Wong TN, Toh KC, Joshi YK. Single-phase liquid cooled microchannel heat sink for electronic packages. Appl Therm Eng 2005;25:1472–87.
[10] Lee H, Agonafer DD, Won Y, Houshmand F, Gorle C, Asheghi M, Goodson KE. Thermal modeling of extreme heat flux microchannel coolers for GaN-on-SiC semiconductor devices. J Electron Packag 2016;138:010907.
[11] Zhou H, Lee J, Kang M, Kim H, Lee H, In JB. All laser-based fabrication of microchannel heat sink. Mater Des 2022;221:110968.
[12] Cheng X, Wu H. Impact of inlet subcooling on flow boiling in microchannels. Exp Therm Fluid Sci 2023;142:110805.
[13] Peles Y, Koşar A, Mishra C, Kuo CJ, Schneider B. Forced convective heat transfer across a pin fin micro heat sink. Int J Heat Mass Transf 2005;48:3615–27.
[14] Wan Z, Joshi Y. Pressure drop and heat transfer characteristics of pin fin enhanced microgaps in single phase microfluidic cooling. Int J Heat Mass Transf 2017;115: 115–26.
[15] Rasouli E, Naderi C, Narayanan V. Pitch and aspect ratio effects on single-phase heat transfer through microscale pin fin heat sinks. Int J Heat Mass Transf 2018; 118:416–28.
[16] Kong D, Jung KW, Jung S, Jung D, Schaadt J, Iyengar M, Malone C, Kharangate CR, Asheghi M, Goodson KE, Lee H. Single-phase thermal and hydraulic performance of embedded silicon micro-pin fin heat sinks using R245fa. Int J Heat Mass Transf 2019;141:145–55.
[17] Woodcock C, Ng'oma C, Sweet M, Wang Y, Peles Y, Plawsky J. Ultra-high heat flux dissipation with Piranha Pin Fins. Int J Heat Mass Transf 2019;128:504–15.
[18] Jung D, Lee H, Kong D, Cho E, Jung KW, Kharangate CR, Iyengar M, Malone C, Asheghi M, Goodson KE, Lee H. Thermal design and management of micro-pin fin heat sinks for energy-efficient three-dimensional stacked integrated circuits. Int J Heat Mass Transf 2021;175:121192.
[19] Zeng L, Deng D, Zhong N, Zheng G. Thermal and flow performance in microchannel heat sink with open-ring pin fins. Int J Mech Sci 2021;200:106445.
[20] Kondo Y, Matsushima H, Komatsu T. Optimization of pin-fin heat sinks for impingement cooling of electronic packages. J Electron Packag 2000;122:240–6.
[21] Sung MK, Mudawar I. Single-phase hybrid micro-channel/micro-jet impingement cooling. Int J Heat Mass Transf 2008;51:4342–52.
[22] Ndao S, Lee HJ, Peles Y, Jensen MK. Heat transfer enhancement from micro pin fins subjected to an impinging jet. Int J Heat Mass Transf 2012;55:413–21.
[23] Han Y, Lau BL, Tang G, Zhang X. Thermal management of hotspots using diamond heat spreader on Si microcooler for GaN devices. IEEE Trans Compon Packag Manuf Technol 2015;5:1740–6.
[24] Jenkins R, Lupoi R, Kempers R, Robinson AJ. Heat transfer performance of boiling jet array impingement on micro-grooved surfaces. Exp Therm Fluid Sci 2017;80: 293–304.
[25] Vutha AK, Rozenfeld T, Shin JH, Rao S, Wang Y, Ziskind G, Peles Y. Spatial temperature resolution in single-phase micro slot jet impingement cooling. Int J Heat Mass Transf 2018;118:720–33.
[26] Cui F, Hong F, Li C, Cheng P. Two-phase flow instability in distributed jet array impingement boiling on pin-fin structured surface and its affecting factors. Int J Heat Mass Transf 2019;143:118495.
[27] Wu R, Fan Y, Hong T, Zou H, Hu R, Luo X. An immersed jet array impingement cooling device with distributed returns for direct body liquid cooling of high power electronics. Appl Therm Eng 2019;162:114259.
[28] Kim J. Spray cooling heat transfer: the state of the art. Int J Heat Fluid Flow 2007; 28:753–67.
[29] Shedd TA. Next generation spray cooling: high heat flux management in compact spaces. Heat Transf Eng 2007;28:87–92.
[30] Tan YB, Xie JL, Duan F, Wong TN, Toh KC, Choo KF, Chan PK, Chua YS. Multi-nozzle spray cooling for high heat flux applications in a closed loop system. Appl Therm Eng 2013;54:372–9.
[31] Jiang LJ, Jiang SL, Cheng WL, Nian YL, Zhao R. Experimental study on heat transfer performance of a novel compact spray cooling module. Appl Therm Eng 2019;154:150–6.
[32] Kim Y, Jung S, Kim S, Choi ST, Kim M, Lee H. Heat transfer performance of water-based electrospray cooling. Int Commun Heat Mass Transf 2020;118:104861.
[33] Wang JX, Li YZ, Zhong ML, Zhang HS. Investigation on a gas-atomized spray cooling upon flat and micro-structured surfaces. Int J Therm Sci 2021;161:106751.
[34] Salman AS, Abdulrazzaq NM, Tikadar A, Oudah SK, Khan JA. Parametric study of heat transfer characteristics of enhanced surfaces in a spray cooling system: An experimental investigation. Appl Therm Eng 2021;183:115824.
[35] Kim SJ, McKrell T, Buongiorno J, Hu LW. Alumina nanoparticles enhance the flow boiling critical heat flux of water at low pressure. J Heat Transf 2008;130:044501.
[36] Ahn HS, Kim H, Jo H, Kang S, Chang W, Kim MH. Experimental study of critical heat flux enhancement during forced convective flow boiling of nanofluid on a short heated surface. Int J Multiph Flow 2010;36:375–84.
[37] Henderson K, Park YG, Liu L, Jacobi AM. Flow-boiling heat transfer of R-134a-based nanofluids in a horizontal tube. Int J Heat Mass Transf 2010;53:944–51.
[38] Lee SW, Kim KM, Bang IC. Study on flow boiling critical heat flux enhancement of graphene oxide/water nanofluid. Int J Heat Mass Transf 2013;65:348–56.
[39] Sun B, Yang D. Flow boiling heat transfer characteristics of nano-refrigerants in a horizontal tube. Int J Refrig 2014;38:206–14.
[40] Zhang C, Zhang L, Xu H, Wang D, Ye B. Investigation of flow boiling performance and the resulting surface deposition of graphene oxide nanofluid in microchannels. Exp Therm Fluid Sci 2017;86:1–10.
[41] Harpole GM, Eninger JE. Micro-channel heat exchanger optimization. In: Proceedings of the 7th IEEE semiconductor thermal measurement and management symposium. IEEE; 1991. p. 59–63.
[42] Wang Y, Ding GF. Experimental investigation of heat transfer performance for a novel microchannel heat sink. J Micromech Microeng 2008;18:035021.
[43] Escher W, Brunschwiler T, Michel B, Poulikakos D. Experimental investigation of an ultrathin manifold microchannel heat sink for liquid-cooled chips. J Heat Transf 2010;132.
[44] Andhare RS, Shooshtari A, Dessiatoun SV, Ohadi MM. Heat transfer and pressure drop characteristics of a flat plate manifold microchannel heat exchanger in counter flow configuration. Appl Therm Eng 2016;96:178–89.
[45] Jung KW, Kharangate CR, Lee H, Palko J, Zhou F, Asheghi M, Dede EM, Goodson KE. Embedded cooling with 3D manifold for vehicle power electronics application: Single-phase thermal-fluid performance. Int J Heat Mass Transf 2019; 130:1108–19.
[46] van Erp R, Soleimanzadeh R, Nela L, Kampitsis G, Matioli E. Co-designing electronics with microfluidics for more sustainable cooling. Nature 2020;585: 211–6.
[47] Dede EM, Joshi SN, Zhou F. Topology optimization, additive layer manufacturing, and experimental testing of an air-cooled heat sink. J Mech Des 2015;137.
[48] Tateishi Y, Parque V, Miyashita T, Gohara H, Kato R, Ikeda Y. Design optimization of heat sink using additive manufacturing. In: Proceedings of the IEEE CPMT symposium Japan (ICSJ). IEEE; 2017. p. 91–4.
[49] Kaur I, Singh P. State-of-the-art in heat exchanger additive manufacturing. Int J Heat Mass Transf 2021;178:121600.
[50] Wauthle R, Vrancken B, Beynaerts B, Jorissen K, Schrooten J, Kruth J-P, Van Humbeeck J. Effects of build orientation and heat treatment on the microstructure and mechanical properties of selective laser melted Ti6Al4V lattice structures. Addit Manuf 2015;5:77–84.
[51] Jafari D, Wits WW. The utilization of selective laser melting technology on heat transfer devices for thermal energy conversion applications: a review. Renew Sustain Energy Rev 2018;91:420–42.
[52] Vyatskikh A, Delalande S, Kudo A, Zhang X, Portela CM, Greer JR. Additive manufacturing of 3D nano-architected metals. Nat Commun 2018;9:593.
[53] Shamvedi D, McCarthy OJ, O'Donoghue E, Danilenkoff C, O'Leary P, Raghavendra R. 3D Metal printed heat sinks with longitudinally varying lattice structure sizes using direct metal laser sintering. Virtual Phys Prototyp 2018;13: 301–10.
[54] Sing SL, Wiria FE, Yeong WY. Selective laser melting of lattice structures: A statistical approach to manufacturability and mechanical behavior. Rob Comput Integr Manuf 2018;49:170–80.
[55] Arie MA, Shooshtari A, Ohadi M. Air side enhancement of heat transfer in an additively manufactured 1 kW heat exchanger for dry cooling applications. In: Proceedings of the 16th IEEE intersociety conference on thermal and thermomechanical phenomena in electronic systems (ITherm). IEEE; 2017. p. 1–8.
[56] Zhang X, Tiwari R, Shooshtari AH, Ohadi MM. An additively manufactured metallic manifold-microchannel heat exchanger for high temperature applications. Appl Therm Eng 2018;143:899–908.

[57] Collins IL, Weibel JA, Pan L, Garimella SV. Evaluation of additively manufactured microchannel heat sinks. IEEE Trans Compon Packag Manuf Technol 2019;9:446–57.
[58] Collins IL, Weibel JA, Pan L, Garimella SV. A permeable-membrane microchannel heat sink made by additive manufacturing. Int J Heat Mass Transf 2019;131:1174–83.
[59] Kempers R, Colenbrander J, Tan W, Chen R, Robinson AJ. Experimental characterization of a hybrid impinging microjet-microchannel heat sink fabricated using high-volume metal additive manufacturing. Int J Thermofluids 2020;5–6:100029.
[60] Nafis BM, Whitt R, Iradukunda AC, Huitink D. Additive manufacturing for enhancing thermal dissipation in heat sink implementation: a review. Heat Transf Eng 2021;42:967–84.
[61] Kong D, Kim Y, Kang M, Song E, Hong Y, Kim HS, Rah KJ, Choi HG, Agonafer D, Lee H. A holistic approach to thermal-hydraulic design of 3D manifold microchannel heat sinks for energy-efficient cooling. Case Stud Therm Eng 2021:101583.
[62] Material data sheet – EOS aluminum AlSi10Mg. Electro optical systems GmbH 2022.
[63] Moffat RJ. Describing the uncertainties in experimental results. Exp Therm Fluid Sci 1988;1:3–17.
[64] Kharangate CR, Wook Jung K, Jung S, Kong D, Schaadt J, Iyengar M, Malone C, Lee H, Asheghi M, Goodson KE. Experimental investigation of embedded micropin-fins for single-phase heat transfer and pressure drop. J Electron Packag 2018;140:021001.
[65] Sharma CS, Tiwari MK, Michel B, Poulikakos D. Thermofluidics and energetics of a manifold microchannel heat sink for electronics with recovered hot water as working fluid. Int J Heat Mass Transf 2013;58:135–51.
[66] Wang Y, Shin JH, Woodcock C, Yu X, Peles Y. Experimental and numerical study about local heat transfer in a microchannel with a pin fin. Int J Heat Mass Transf 2018;121:534–46.
[67] Pan YH, Zhao R, Fan XH, Nian YL, Cheng WL. Study on the effect of varying channel aspect ratio on heat transfer performance of manifold microchannel heat sink. Int J Heat Mass Transf 2020;163:120461.
[68] Tang J, Li X, Hu R, Mo Z, Du M. A novel designed manifold ultrathin micro pin-fin channel for thermal management of high-concentrator photovoltaic system. Int J Heat Mass Transf 2022;183:122094.
[69] Dhinsa K, Bailey C, Pericleous K. Low Reynolds number turbulence models for accurate thermal simulations of electronic components. In: Proceedings of the 5th international conference on thermal and mechanical simulation and experiments in microelectronics and microsystems; 2004. p. 483–90. 2004. EuroSimE 2004. Proceedings of The, IEEE.
[70] Dhinsa K, Bailey C, Pericleous K. Investigation into the performance of turbulence models for fluid flow and heat transfer phenomena in electronic applications. IEEE Trans Compon Packag Technol 2005;28:686–99.